Version of Record: https://www.sciencedirect.com/science/article/pii/S1290072922004094
Manuscript_5fb48fa35d6ba634044736360d32cb65

Atomic Layer Thermopiles: Comprehensive Static Calibration, Comparison and Application in Subsonic and Supersonic Flows

Konstantin Huber[a], Tim Rödiger[a], Lakshya Bhatnagar[b], Guillermo Paniagua[b]

[a] *UAS Landshut - Thermal and Fluid Mechanics Lab, Am Lurzenhof 1 , Landshut, 84036, Bavaria, Germany*
[b] *Purdue University - Experimental Turbine Aerothermal Lab, 500 Allison Road, West Lafayette, 47907, IN, USA*

Abstract

This paper compares the calibration of different heat flux sensors in radiation- and convection-based sub- and supersonic operation. First, four heat flux sensors based on different principles: ALTP (Transverse Seebeck Effect), HFM-8E (differential-layer device), coaxial Thermocouple and a TG-2000 (circular-foil gage) are calibrated in a laser-based radiation setup. In a second step, all heat flux sensors are compared with a slug-calorimeter within a subsonic convection-dominated facility based on stagnation-point measurements of an impinging hot air jet. The obtained results indicate that a sensitivity transfer between a radiative calibrated sensor used in a mainly convective environment is not always possible and can lead to significant, systematic errors. Calibration in a subsonic shear flow with thermocouple readings demonstrate small divergence from the manufacturer provided sensitivity. Finally, supersonic testing with high frequency shock-boundary layer interactions highlight the need for ALTP rather than the conventional use of thermocouple arrays to resolve the high frequency phenomena associated with shock boundary layer interactions.

Keywords: Convective Heat Flux Measurement, Sensor Calibration, Radiation, Thermopile, High Speed Flow Measurements, Instrumentation

Nomenclature

α_a	Absorption coefficient
ΔS	Difference of the Seebeck coefficents
ΔS_{man}	Temperature depending sensitivity change provided by manufacturer

Email address: konstantin.huber@haw-landshut.de (Konstantin Huber)

ΔT	Temperature difference
Δt	Time interval
ϵ	Spectral emissivity
γ	Tilt angle
λ	Wavelength
$\rho c_{\mathrm{p}} k$	Thermal product
C	Individual uncertainty
D	Nozzle diameter
HCP	Heat conducting paste
HFS	Heat flux sensor
H	Horizontal distance nozzle/baffle plate
R	Radial distance to stagnation point
TC	Thermocouple
TSE	Transverse Seebeck Effect
A	Surface area
a	Linear fitted slope
b	Linear fitted intercept
c_{p}	Specific heat capacity
d	Thickness
k	Thermal conductivity
l	Length
m	Mass
n	Number of samples
Q	Heat Flux density
Q_{st}	Heat Flux density at stagnation point
S_{exp}	Sensitivity experimentally determind
S_{man}	Sensitivity provided by manufacturer
s_q	Sample average square of heat flux deviations

s_u	Sample average square of voltage deviations
t_α	Student t distribution factor
t_n	Specific time step
T_w	Wall-temperature
U	Voltage/Flow velocity

1. INTRODUCTION

Understanding of internal flows require precise high frequency heat transfer measurement as evident in a wide variety of applications [1, 2, 3, 4]. Wall-mounted heat flux gages such as thermocouples, thin-films, differential-layer devices, etc. are generally used. Optical methods do not reach sufficient levels of accuracy and spectral resolution. Micro-thermocouples and thin films require numerical signal processing algorithms [5, 6, 7] to achieve kHz frequency response. Unfortunately, the inherent strong numerical noise limits the temporal resolution. Differential-layer devices based on the Transverse Seebeck Effect offer higher temporal resolution such as the Atomic Layer Thermopile (ALTP) with a time constant in the microsecond range [8, 9, 10] and the Heat Flux Microsensors (HFM) series [11] with a time constant in the tens of microseconds range. Calibration is required in order to determine the static sensitivity [12, 13, 14, 15, 16, 17, 18], the dynamic response time [19, 20] and the dynamic amplitude-frequency response [9, 10, 21, 18].

Moffat [13] noted that errors in heat flux sensors of $\pm\,10\%$ are reasonable. The abatement of the calibration uncertainty is essential for accurate data [10, 22].

Heat flux sensor calibration is carried out using a single heat transfer mechanism: a purely radiation-based or (mainly) convection-based procedure. The validity of the determined sensitivity for the other or mixed heat-transfer mechanism is not evident and studies that compare sensitivities for different calibration mechanisms and fast-response sensors are scarce.

In this paper, the calibration of different heat flux gages in two different environments, a radiation-based setup and one mainly convection-driven, are investigated and compared. For absolute heat flux sensor calibration most commonly radiation-based procedures are used: The National Institute of Standards and Technology (NIST) uses a variable-temperature blackbody as a broadband radiant source [14, 15, 16]. The calibration setup transfers the readings of a primary electrical substitution radiometer to calibrate heat flux sensors up to $50\,\mathrm{kW\,m^{-2}}$. Although there are different radiative calibration methods, reported errors are often in the low percentage region ($1-3\,\%$) [23, 24] for different types of sensors, making these radiation calibration techniques ideal for absolute calibration.

Previous studies showed that individual calibrations for each single heat flux sensor are always necessary prior usage because of tolerances in the manufacturing process [12]. For this purpose a less expensive substitution calibration is widely used in industry and research: Each single sensor to be calibrated and a reference gage are successively exposed to a repeatable heat flux source from a laser, a fluid flow or a broadband source, to then refer the measured heat flux value of the reference gage to the output voltage of the sensor to be calibrated.

Among others, Borell and Diller [12] showed in an experimental analysis of a circular-foil gage (calibrated in a radiation-based calibration procedure) as well as Fu et al. and Yang [25, 26] in a theoretical analysis that this type of sensor requires correction to the calibration, if it is used in a convective and mixed convective and radiative environment. This result suggest that all heat flux sensors calibrated with irradiation should be additionally evaluated in a convective environment.

An absolute convection-driven calibration procedure is proposed by Borrell and Diller [12]. They make use of an impinging free air jet (at room temperature) on a guarded hot plate apparatus. In general, absolute convective calibration is prawn to many uncertainties e.g. by the fluid flow characteristics (relevant turbulence level, temperature distribution etc.). For the convective case, several authors [7, 13, 19, 27] already described the absolute convection calibration in subsonic flow is difficult and reported errors in the order of $\pm\,10\,\%$. However, if the stagnation point region of a hot air jet offers a fairly constant heat flux distribution it can be used as an environment for a substitute convective calibration, to evaluate and compare heat flux sensors in the stagnation area.

A comparative study of different heat flux sensors in supersonic and hypersonic facilities are shown in [18, 28] including several of the current sensor types. Here different geometries (multiple blunt body probes or flat plate boundary layer, respectively) are used for simultaneous comparison of different heat flux sensors. The study shows good agreement, however the accuracy and repeatability is limited ($5-30\,\%$) due to changing reservoir conditions, flow inhomogeneity and/or particle impacts.

In the following different heat flux sensors based on different principles: ALTP (Transverse Seebeck Effect), HFM-8E (Differential Layer, a TG-2000 (Circular Foil) are first calibrated in the same radiation-based calibration setup and compared to the manufacturers' calibration. In a second step, all sensors are initially compared with coaxial thermocouples, manufactured by Mueller Instruments [29] and a slug-calorimeter using the stagnation region of a subsonic hot air jet and in a shear layer calibration facility, the ALTP is compared with a temperature based reference heat flux determination. In a third step, the ALTP is assessed in a supersonic test case consisting of a linear representation of a supersonic bladeless turbine at Mach 2 in comparison to heat flux calculated from surface thermocouples.

2. HEAT FLUX SENSORS USED IN CALIBRATION

The following heat flux/temperature gauges are chosen for quantitative comparison that are typically found in different fields: coaxial thermocouples are commonly used in high-speed flows, flow transitions and combustion investigations, HFM-8E sensors are applied in gas turbine blade studies, TG-2000 sensors investigate radiation heat transfer and broadband flame-radiation measurements. Calorimetric gauges are used in most heat-transfer investigations due to its simplicity. The selected techniques allow a comprehensive comparison for several heat transfer applications.

Atomic Layer Thermopiles (ALTP) are heat flux sensors based on the Transverse Seebeck Effect (TSE). The sensor consists of a several hundered nanometer thick, tilted layered structure which is made of Yttrium-Barium-Copper-Oxide (YBCO) and CuO_2 grown on a $SrTiO_3$ cylindrical substrate. Based on the TSE, an electrical field is created if a temperature difference $\Delta\,\mathrm{T}$ across the tilted stucture (active layer) is present [30]. The measured output voltage $\mathrm{U_{ALTP}}$ is generated by the active layer (Figure 1a),

$$\mathrm{U_{ALTP}} = \frac{l\,\sin 2\gamma\,\Delta S\,\Delta T}{2\,d} \tag{1}$$

where l is the length of the active film, γ is the tilt angle, d is the thickness of the active film and ΔS the diffence of the Seebeck coefficients of the two materials. The sensors output voltage is directly proportional to the impinging heat flux over 11 orders of magnitude [31]. Through its thin semi layer design theoretical response times in the several nanoseconds range can be reached [30].

The ALTP sensor used in this paper is mounted in a ceramic housing with an outside diameter of 8 mm, the front diameter of the $SrTiO_3$ cylindrical substrate is $3-6\,\mathrm{mm}$. The active layer size is about $3\times 2\,\mathrm{mm}^2$. For electrical connection gold contacts on two opposite sides are used. The manufacturer (FORTECH HTS [32]) of the sensor provides a static sensitivity of $104\,\mu\mathrm{V\,cm^2\,W^{-1}}$ with an uncertainty of $\pm\,20\,\%$ obtained from radiation-based calibration. The power meter used in the calibration setup for determining the incident laser power is calibrated by PTB (Physikalisch technische Bundesanstalt) and NIST traceable. On top of the surface of the active film and gold contacts an additional coating is deposited that allows for maximum absorption (approx. $99\,\%$) at $\lambda = 10.6\,\mu\mathrm{m}$ wavelength. The coating also leads to longer recalibration intervals of the sensor (approx. up to one year) because the active layer of the ALTP is hygroscopic and also leads to higher robustness for usage in harsh environments. Applying the coating reduces the time constant by a factor of $2-3$, a sensor without coating requires a recalibration within several months due to possible changes of the sensitivity by possible water absorption [17].

The sensor dynamics where already studied by [9, 10, 18, 32] based on amplitude-frequency response characteristics obtained from modulated laser calibrations. They show the ALTPs dynamics in a frequency range up to 1 MHz. The response curve allows signal correction across the entire frequency range

and makes the ALTP the fastest heat flux sensor (time constant 1 µs) currently commercially available.

Heat Flux Microsensors (HFM) are differential-layer devices with an exactly known electrically and thermally insulating layer in-between a thermopile (see Figure 1b). The thermopile consists of many pairs of differential thermocouples (TC) connected in series. The voltage output, produced by small temperature differences across the insulating layer is directly proportional to the impinging heat flux through the entire sensing area [20]. In order to compensate the temperature depending sensitivity of the HFM-8E, there is a temperature measuring TC directly integrated in the body of the sensor, the exact position of the TC is unknown. The sensor is mounted in a metallic housing with an outside diameter of 6.35 mm. The front active side of the sensor (5.8 mm) is coated with black paint with a known emissivity of 0.95 [11]. Recent studies concerning the Pyromark 1200 painting show lightly varying results of the emissivity coefficient $\epsilon > 0.9 - 0.93$ for $\lambda = 3 - 14\,\mu\text{m}$ [33, 34].

The manufacturer (VATELL [11]) of the sensor provides a static sensitivity of $576\,\mu\text{V}\,\text{cm}^2\,\text{W}^{-1}$ obtained from radiation-based calibration at $30.8\,\text{W}\,\text{cm}^{-2}$. The calibration is NIST traceable according to the manufacturer at a listed maximum operation temperature of 350°C. A response time estimation of 17 µs (uncoated)/300 µs (coated) is provided in the manufacturers manual[11] without any precisely determined amplitude frequency response for the specific sensor.

Calorimeters are a very fundamental, robust and simple heat flux measurement technique. The calorimeter used here is composed of a copper mass/slug with a high thermal conductivity mounted in a insulating housing made of PTFE. This material combination results into a Biot-number < 0.1 (comp. Figure 1c) and the sensor can be modeled as a lumped capacitance. Thus, by measuring the temperature rise of the slug within a certain period of time, the mean heat flux density within the time interval can be calculated by

$$Q = \frac{m_{\text{Cu}} \cdot c_{\text{p}} \cdot (T_{\text{start}} - T_{\text{end}})}{A_{\text{sur}} \cdot \Delta t} \tag{2}$$

where Δt is the measuring time interval, A_{sur} the wetted surface area of the slug, m_{Cu} is the mass of the slug, c_{p} is the temperature dependent heat capacity between the start T_{start} and end temperature T_{end}.

The measurement principle shows that the temporal resolution is very low and largely depends on the dimensions and mass of the device. In addition, the accuracy is strongly dependent on the time interval and temperature history. The calorimeter used in this paper is especially designed for the determination of the mean heat flux densities and the flow characteristics in the convection-based calibration procedure. Conductive losses to the wall are theoretically estimated and accounted for. The calorimeter is composed of a cylindrical copper slug with a diameter of 9.7 mm and with a total mass of 3280 mg. The slug is mounted in a high temperature plastic housing with an outside diameter of 16 mm. The temperature is directly measured on the rear side by an insulated type K thermocouple. The TC is submerged in the center of the circular, rear

surface and heat conducting paste is used to ensure proper thermal connection to the slug. The voltage of the thermocouple is recorded (21 kHz) and the minimum (prior heat exposure) and maximum temperature (after the end of the exposure) are extracted from the temporal history (10 Hz-filtered by a numerical running-mean filter) as well as the time interval between them. The sensitivity of the type K thermocouple is NIST traceable, the designed calorimeter as heat flux sensor is not NIST traceable.

Circular foil gages use a very thin active layer (circular foil) made of constantan acting as a differential constantan-cooper thermocouple (cooper block and cabels comp. Figure 1d) [35]. The massive copper block helps to conduct the impinging heat flux towards the outside diameter and generates a differential temperature between the inner circle point and the outer diameter. The output voltage of this thermocouple is direct proportional to the incident (radiant) heat flux. It was found that circular foil gages are especially suitable for the precise determination of radiant heat fluxes. For use in convection-driven environments, a correction of the calibration is needed [12, 25]. The response time of this very robust measurement technique can be at the most in the order of milliseconds [36].

The exact circular foil gage used in this paper is a TG-2000 produced by Vatell[37]. The front side surface of the sensor ($\varnothing \approx 12.7\,\mathrm{mm}$) is coated with a black paint (Pyromark) with a emissivity of 0.95 (same as HFM-8E). The manufacturer of the sensor provides a static sensitivity of $320\,\mu\mathrm{V\,cm^2\,W^{-1}}$ with an uncertainty of $\pm\,3\,\%$ obtained from radiation-based calibration. The calibration is NIST traceable according to the manufacturer. A maximum heat flux density of $5000\,\mathrm{W\,cm^{-2}}$ is given.

Coaxial Thermocouples are temperature-based heat flux measuring techniques using a one-dimensional transient conduction analysis in order to determine the wall heat flux time history. They are composed of a central thermocouple material that is electrically insulated from the outer one. The elements are connected on the surface either by vacuum deposition or removal of the insulation between the two metals by merging or grinding. In this study, a coaxial thermocouples of type E (Chromel/Constantan) MCT-19 manufactured by Mueller Instruments [29] is used. The thermocouple (comp. Figure 1e) consist of one element that is swaged over the other with a 10 µm electrical insulation between them. To ensure firm installation, the metal housing of the thermocouple with an outer diameter of 1.9 mm is threaded into the wall and the surface is grinded to fit and flush mount it to the surface. The created microscratches form at the same time the junction of the thermocouple. Because of this very thin thermocouples junction a temporal resolution of the temperature time history in the order of microseconds is reached [38].

The manufacturer provides a static sensitivity of about 59.6 $\mu\mathrm{V\,K^{-1}}$ at 20 °C. This temperature sensitivity is NIST traceable according to the manufacturer and for more precise evaluation a NIST proposed inverse coefficients polynomial approximation for type E thermocouples is used here. A heat flux density range between $20\,\mathrm{kW\,m^{-2}}$ to $20\,\mathrm{MW\,m^{-2}}$ is given and a operation temperature range between -200 to 900 °C is listed. For proper heat flux calibration in the radiative

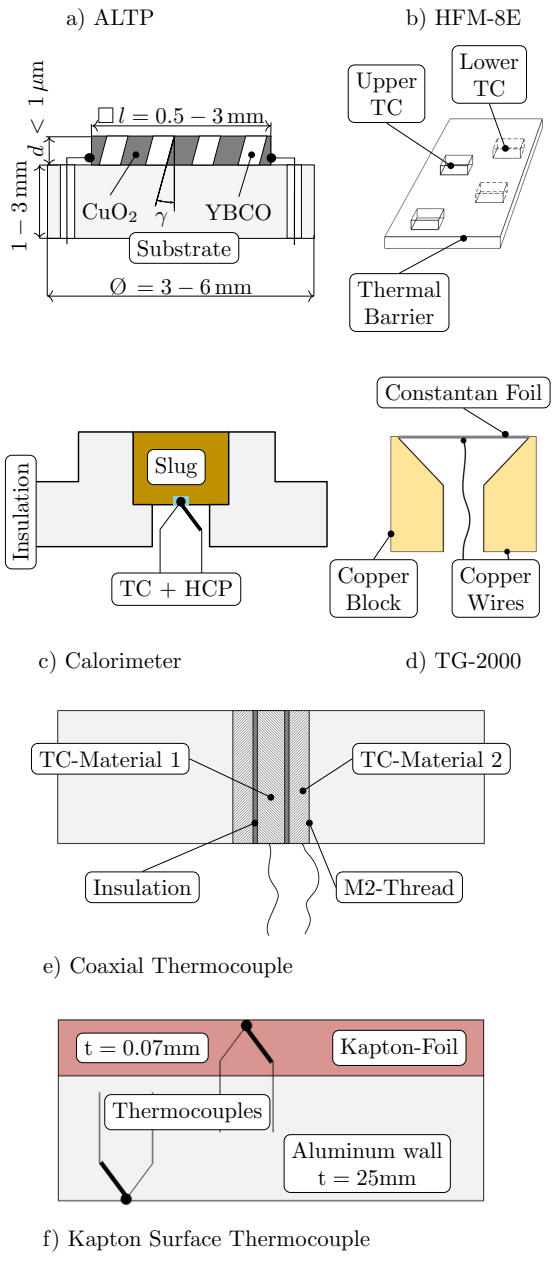

Figure 1: SCHEMATIC OF DIFFERENT HEAT FLUX SENSORS: a) ALTP, b) HFM-8E, c) CALORIMETER, d) TG-2000, e) COAXIAL THERMOCOUPLE, f) KAPTON SURFACE THERMOCOUPLE.

environment, the coaxial thermocouple was coated with Pyromark 1200.

With the knowledge of the sensor material given as the thermal product $\left(\sqrt{\rho\, c_p\, k}\right) = 8653\,\sqrt{s\,m^{-2}\,K^{-1}}$ the heat flux into the sensor can be calculated based on the "semi-infinite wall" assumption. This assumption is only valid as long as the back side of the thermocouple does not heat up. According to the manufacturer, the largest error of the sensor results from the calibration of the thermal product with an uncertainty of $\pm 3.5\,\%$. This calibration procedure is not NIST traceable. In this study the mostly known Cook-Felderman (CF) algorithm [5] is used for heat flux calculation.

Kapton surface thermocouples are also temperature-based measurement devices. The bottom temperature represents the temperature of the thick aluminum wall. By using a differential approach between the top side temperature (temperature of the thin Kapton layer) and the bottom side temperature (temperature of the thick aluminum wall), a heat flux can be derived. For this device, it is done by making use of a numerical finite volume method based on a one-dimensional approach with a Crank Nicholson discretization scheme. Therefore, the thermal parameters of the involved materials have to be known. A more detailed description of the numerical procedure can be found in [39]. An uncertainty analysis can be found in the shear flow convection section. For the temperatures, a NIST proposed inverse coefficients polynomial approximation is used. The Kapton foil should be as thin as possible for low response times. The assumed response time is several 100 microseconds [40].

Measurement process and data acquisition for the subsonic investigations consists of low noise optimized operational amplifiers with precisely determined gain factors. The sampling rate of 21 kHz was chosen depending on the capabilities of the operational amplifiers which are limited by the usable bandwidth of approx. 7 kHz (-3 dB)) at high gain factors and by use of filter systems. The HFM-8E and the TG2000 are measured with the AMP-13 amplifier system provided by the manufacturer. The signal filtering was implemented based on a third order Butterworth low-pass filter (-3 dB-cutting edge) of 7 kHz. The analog-to-digital conversion was done with a PicoScope 5443d and a Rigol MSO 5074 oscilloscope with noise-level depending grounding. The ground noise level differs slightly for different sensors and measuring environments. For the supersonic investigations in the LEAF facility, the signals are recorded with 128 kHz sampling rate also based on an operational amplifier with precisely determined gain factor.

3. CALIBRATION PROCEDURES

Radiation-based calibration procedure

The radiation-based calibration procedure intends to relate the absorbed power of a laser beam with a measured heat flux density by a reference meter. The setup (Fig.2) consists of a CO_2-laser that emits monochromatic light at 10.6 µm, a microlens array for beam profile homogenization and an attenuator for the variation of the laser power. With an accurate calibrated power meter

(PM) placed behind an adaptable aperture, the reference heat flux density can be exactly applied to the specific surface of the heat flux sensor (HFS). The intensity can be varied between $0.5-12\,\mathrm{W\,cm^{-2}}$ for the employed beam-aperture configuration. The precision fabricated metal grids inside the attenuator diffract a known percentage of beam power which is absorbed by the wall. By means of six different attenuator elements, different load stages for sensor calibration can be provided. The microlens array is especially optimized for the wavelength of the CO2-Laser. By using the beam-homogenization array, the intensity profile can be distributed homogeneously over the beam. The quality of the resulting intensity profile depends on the incoming beam and the final uniformity of the beam is significantly improved and estimated to be approximately 10 %. All HFS are placed behind the circular aperture in order to obtain a well defined reference cross section A_{ref}. The maximum active area of the sensors are always smaller than this reference area of the laser beam. Therefore, the sensor could be totally exposed to an incident radiation of known intensity i. The beam intensity $i = P_{\mathrm{laser}}/A_{\mathrm{ref}}$ can be determined with the power of the dissected laser beam P_{laser}, measured by a commercially available power meter (PM) with PTB calibration. The accuracy of the power meter is specified as $< 1\,\%$.

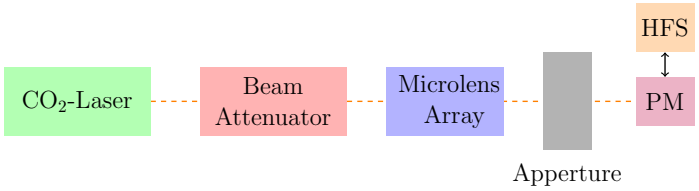

Figure 2: SCHEMATIC ILUSTRATION OF THE LASER-CALIBRATION FACILITY.

An accurate calibration process can only take place if the optical properties of the sensors surfaces are known for the wavelength/spectrum of the incident radiation. This is the reason why only heat flux sensors with special coating (see Instrumentation section) with known optical properties are selected for the radiation-based calibration. The accuracy of the resulting absorption coefficient α_{a} is in the range $< 10\,\%$.

The resulting sensor voltage signals U_{meas} of the heat flux sensors are amplified, the uncertainty of the measured voltage U_{meas} including the respective gains of the amplifiers is estimated with 2 %. The uncertainty of the non-uniformity of the laser beam is determined by a slot aperture as discussed in [17].

Table 1: UNCERTAINTY EVALUATION OF RADIATION-BASED CALIBRATION PROCEDURE.

$\frac{\Delta\alpha_{\mathrm{a}}}{\alpha_{\mathrm{a}}}$	$\frac{\Delta A_{\mathrm{ref}}}{A_{\mathrm{ref}}}$	$\frac{\Delta U_{\mathrm{meas}}}{U_{\mathrm{meas}}}$	$\frac{\Delta P_{\mathrm{laser}}}{P_{\mathrm{laser}}}$	$\frac{\Delta P_{\mathrm{laser}}}{P_{\mathrm{laser}}}$ (uniformity)
10%	0.01%	2%	1%	10%

The slope of the curve resulting from the measured sensor voltage versus the variation of intensity by the attenuator delivers the sensitivity (comp. Fig.9). The total uncertainty of the calibration can be estimated from (Equation 3) defining the sensitivity coefficient:

$$s = \frac{U_{\text{meas}}}{\alpha_{\text{a}}\, i} = \frac{U_{\text{meas}}\, A_{\text{ref}}}{\alpha_{\text{a}}\, P_{\text{laser}}} \tag{3}$$

By differentiating this expression and adding the RMS-values of all single, conservative estimations of uncertainties listed in Table 1, leads to an overall uncertainty in the calibration of $< 14\,\%$.

Stagnation point convection-based calibration procedure

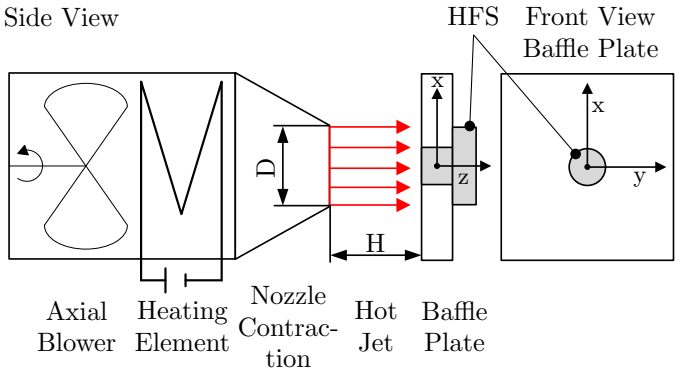

Figure 3: SCHEMATIC ILLUSTRATION OF THE CONVECTION CALIBRATION FACILITY.

The convection calibration is a substitute procedure in the stagnation-point region of an hot, impinging air jet. Substitution means exchanging sensors during the same operation cycle and comparing the calculated results based on sensor specific sensitivity which was obtained beforehand from an absolute calibration procedure (e.g. radiation-based, see above). Hence, only relative comparisons between different heat flux sensors are possible. The convection-based setup (Figure 3) uses a high-power (10 kW) heater in combination with an axial blower to deliver air at approximately 700 °C. A circular cross section nozzle contracts the air to a free jet with an exit diameter of D = 48 mm. The free jet impinges in the center of a baffle plate which is adjusted to be perpendicular to the axis of the free jet. Both the heater-blower unit and the baffle plate are mounted on a linear rail system that allows the precise variation of the axial distance H between the nozzle exit and the plate. For small H, maximum heat flux densities of approximately $10\,\mathrm{W\,cm^{-2}}$ can be reached, matching the calibration range of the radiation-based procedure (see above). The baffle plate is made out of high conducting aluminum and its temperature is monitored during the operation to deliver boundary conditions as constant as possible.

A shutter system installed between the nozzle and the plate limits the exposure time of HFS mounted in the plate in order to prevent long term exposure and their temperature overload. Typical exposure times of the sensors are in the second range. The quality of the procedure largely depends on its repeatability for successive sensor exposure, as well as the homogeneity of the heat flux distribution in the stagnation area because most heat flux sensors feature different active film sizes. The repeatability and the homogeneity is measured for a fixed distance H/D = 5 and the results are shown in Figure 4 and 5.

The repeatability is studied after an initial warming-up phase of the setup by a calibrated ALTP that is mounted in the stagnation point and successively exposed to the free jet. The measurement was repeated 20 times with an interval of 60 seconds between the measurements. During the measurements, the ambient (room) temperature is monitored because the ambient air mixes into the free shear layer of the hot-air jet. The room temperature increased by approximately 10 K which is about 1.5 % in reference to the jet temperature. This ambient temperature change could not be directly correlated with the upward drift of the measurement data set in Figure 4. The figure shows that a mean heat flux density of 7.3 $\mathrm{W\,cm^{-2}}$ is measured for 20 repetitions with 95 % confidence interval of $\pm\,0.25\,\mathrm{W\,cm^{-2}}$ or 3.6 % of the mean value. Moffat and Danek [13] estimated a repeatability uncertainty of ±2 % for convective environments, Borell and Diller [12] measured a 1.9 % repeatability within a 95 % confidence interval which matches our observed results.

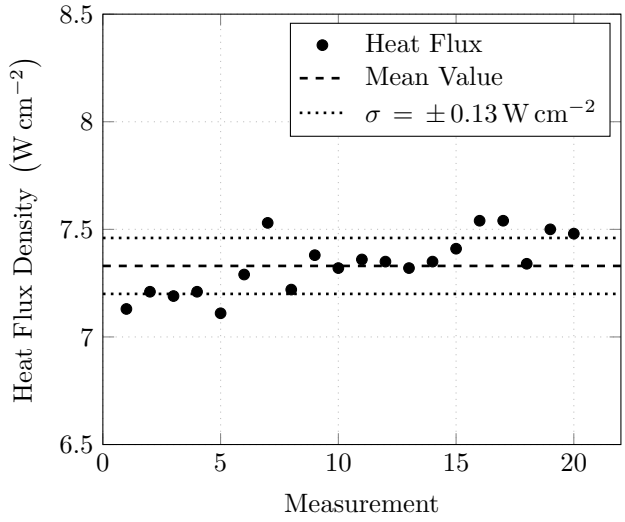

Figure 4: MEASURED HEAT FLUX DENSITIY WITH ALTP SENSOR IN THE STAGNATION POINT AT H/D = 5 WITH 20 REPETITIONS - STANDARD DEVIATION $\sigma = \pm\,0.13\,\mathrm{W\,cm^{-2}}$.

The homogeneity of the stagnation-point area at the baffle plate is studied by traversing it with an installed, calibrated ALTP sensor in horizontal and

vertical direction in 1.6 mm steps, respectively. Figure 5 displays both profiles in non-dimensional R/D coordinates where radial distance R is the distance of the sensors current location compared to the central mounting point in the stagnation region (R = 0). In addition, the active film areas of all heat flux sensors (ALTP, HFM-8E, TG-2000, TC), are marked in the same diagram. The active area of the ALTP is $3 \times 2 = 6\,\mathrm{mm}^2$ compared to the HFM-8E with $\approx 30\,\mathrm{mm}^2$ and the TG-2000 with $\approx 125\,\mathrm{mm}^2$ (coated areas are assumed as active films, no other detailed information is given by manufacturer). For the sensor with the largest front surface (TG-2000), the maximum standard deviation of the heat flux density in horizontal direction is $0.1\,\mathrm{W\,cm^{-2}}$ or 1.3 % of the mean value in the area, and in vertical direction $0.05\,\mathrm{W\,cm^{-2}}$ or 0.65 % of the mean value. The homogeneity and repeatability investigations show that the stagnation-point area offers a sufficiently constant heat flux density in order to carry out successive, comparative measurements of heat flux sensor with different active areas.

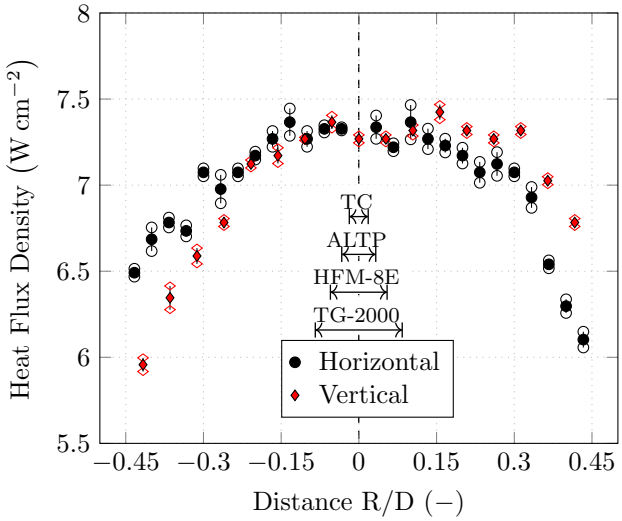

Figure 5: HOMOGENEITY OF THE IMPINGING FLOW FOR VARIED R/D-DISTANCES IN HORIZONTAL AND VERTICAL DIRECTION AT H/D = 5. ERROR INCIDENCES REPRESENTS THE STANDARD DEVIATION σ FOR FIVE MEASUREMENTS AT EACH POINT.

For the comparison of sensors with different temporal resolutions it can be important to quantify the uncertainty of the free hot air jet in terms of its fluctuations and turbulence. Thus, a spectral analysis of the measurement signals of the ALTP, HFM-8E, TG-2000 and the TC are evaluated for a fixed H/D = 5. An averaged spectral density is shown in Figure 6 for each sensor. The ALTP and the HFM-8E spectra show a good agreement in the low-frequency range which is relevant for the convective comparison of the mean values. In the kHz-range the spectrum of the ALTP decays at a later point. In addition, the

spectra display the noise floor that is calculated from the signals before exposure for each sensor. It should be noted that the data for the ALTP spectrum in Figure 6 is measured with a different amplifier without a low-pass filter and a −3 dB-bandwidth of 1.3 MHz. It consists of an instrumentation amplifier with a gain of 1000 (60 dB) and an specified input noise of 1 nV $\mathrm{Hz}^{-0.5}$. For the HFM-8E the amplifier produced by the manufacturer (AMP-13) at Gain 100 is used. The bandwidth of the TG-2000 is much lower which can be explained by its lower time constant.

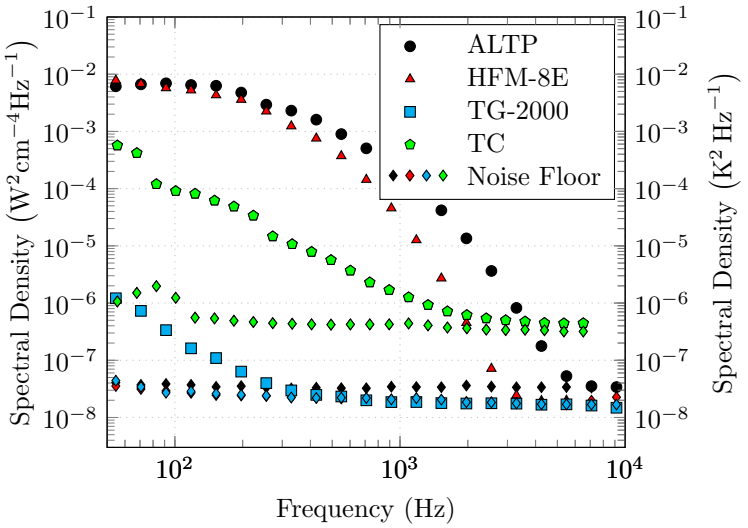

Figure 6: SPECTRAL DENSITY OF THE FREE JET EVALUATED FOR THE ALTP, HFM-8E, TG-2000 AND THE COAXIAL TC.

The spectrum of the TC calculated from the temperature time signal (not heat flux) is show in addition in the same diagram (right axis). The temperature fluctuations show a similar frequency range as the spectra of heat flux fluctuations of the ALTP and the HFM-8E. For the spectral analysis, all signals are captured with a sampling rate of 100 kHz. The spectral analysis delivers RMS-values of 1.8 W cm^{-2} (ALTP), 1.6 W cm^{-2} (HFM-8E), 0.1 W cm^{-2} (TG-2000) and 1.0 K (TC).

The free-jet setup can be furthermore used to produce relative, convective calibration curves by varying the distance H of the baffle plate and the nozzle exit. With increasing H, more ambient (cold) air is mixed into the shear layer of the free hot-air jet. Thus, the mean temperature of the jet decreases with increasing H and also the impinging mean heat flux density in the stagnation area. It has to be noted that the mixed-in cold air also transforms the heat-density profile and the homogeneity significantly decrease with H. Therefore, the values given in Figure 5 and 12 for a fixed H/D = 5 do not apply for such a curve. However, this variation and its resulting calibration curve (comp. Fig. 13) allow the comparison of heat flux sensors for different convective heat

flux densities. Such curves can give an indication for heat flux density and/or temperature dependent deviations of different heat flux sensor readings.

Shear flow convection-based calibration

The shear flow based calibration was carried out at the Linear Experimental Aerothermal Facility (LEAF), located at Purdue University[41]. LEAF is a linear blowdown facility that flows air from pressurized tanks to a vacuum dump tank. It consists of a settling chamber, the linear test section and a sonic valve to set the Mach number. The details of operation are documented in [42, 43].

For the LEAF measurements, a different ALTP sensor due to significant different mounting, noise level and response time demands was used. This sensor has a different active length and film thickness to meet the requirements, flow regimes etc. This leads according to Equation 1 to a different output voltage and therefore to different sensor sensitivities. In order to enable a comparison between all investigated facilities, both ALTP sensors are calibrated in the same radiation-based facility (see section Calibration Procedures). The results indicated a sensitivity of 59 µV cm^2 W^{-1}. Typical ALTP sensitivities can be in the range of 20–150 µV cm^2 W^{-1}.

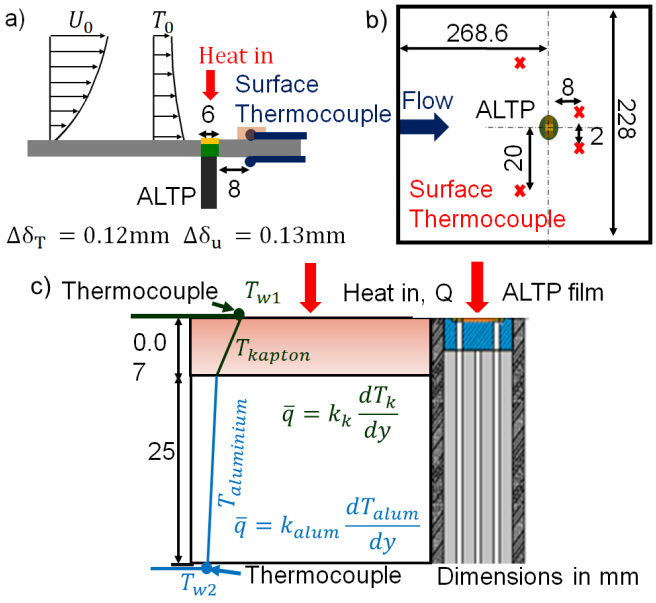

Figure 7: a) SHEAR FLOW CALIBRATION SETUP b) LAYOUT OF THE SENSORS IN THE TEST SECTION c) SCHEMATIC OF THE HEAT FLUX CALCULATION FROM THE SURFACE THERMOCOUPLES.

The ALTP sensor is placed on the top wall of the LEAF linear test section along with an array of surface thermocouples which are sub-millimeter, thin wire thermocouples. Physically, there is a axial and spanwise difference in the

position of the two sensors to ensure that the boundary layer is not disturbed for one sensor due to the presence of the other. Figure 7 a) shows the operational principle and 7b) shows the layout of the sensors with reference to the start of the test section.

The difference in the boundary layer and thermal boundary layer between the ALTP and the surface thermocouple is 0.13mm ($\approx 3\,\%$) and 0.12mm ($\approx 3\,\%$) respectively at a representative calibration condition [44]. This leads to a difference in the heat load of 0.58 %, for the two sensors which is within the uncertainty of the heat flux calculation method. The methodology presented in [39] is used to convert the surface thermocouple readings into heat flux. The schematic of the problem is shown in Figure 7c), the test plate is instrumented with surface thermocouples on the inner surface (exposed to the fluid flow) and on the outer surface (exposed to ambient). The inner surface thermocouple is mounted on a layer of Kapton, and the plate is made of aluminium. The temperature readings are converted to heat flux through a numerical solver [39] for the 1D unsteady state heat conduction given by Equation 4. Heat flux continuity, given by Equation 5, is applied at the interface of the two layers. The solver uses a Crank Nicholson discretization scheme and was validated against an analytical solution [39].

$$\frac{\partial T}{\alpha \partial t} = \frac{\partial^2 T}{\partial x^2} \tag{4}$$

$$-k_1 \frac{\partial T}{\partial x}_{x=L+} = -k_2 \frac{\partial T}{\partial x}_{x=L-} \tag{5}$$

The uncertainty on the heat flux was assessed through a parametric sensitivity, shown in Table 2, where the heat flux calculation is performed by adding the uncertainty for each parameter. Here, sensitivity is defined as the percentage change in heat flux for a 100 percent change in input parameter. This is based on the work of Saavedra et al. [39]. The uncertainty for each parameter was

Table 2: UNCERTAINTY ON HEAT FLUX ESITMATION.

Parameter	Value	Units	Uncertainty	Sensitivity
δ_{Kapton}	0.07	mm	0.01	77.3 %
$\delta_{\text{Aluminium}}$	24.76	mm	0.01	171.7 %
ρ_{Kapton}	1420	kg m^{-3}	0.71	145 %
$\text{C}_{\text{p Kapton}}$	1090	$\text{J kg}^{-1}\,\text{K}^{-1}$	10.9	15 %
k_{Kapton}	0.12	$\text{W m}^{-1}\,\text{K}^{-1}$	0.0036	79.7 %
$\rho_{\text{Aluminium}}$	2700	kg m^{-3}	108	2.7 %
$C_{\text{pAluminium}}$	897	$\text{J kg}^{-1}\,\text{K}^{-1}$	27	0.9 %
$k_{\text{Aluminium}}$	180	$\text{W m}^{-1}\,\text{K}^{-1}$	7.2	13.6 %
T_{front}	317.8	K	0.31	549.4 %
T_{back}	314.2	K	0.31	549.4 %
Heat Flux	0.95	W cm^{-2}	Uncertainty	11.3 %

taken for a 95 % confidence interval based on literature or measurements. The final uncertainty on heat flux is estimated through the methodology of Moffat [45]. From the table it is evident that the heat flux calculation is more sensitive to the properties of the Kapton tape than of the aluminum insert, hence a greater accuracy is required to characterize the properties of the Kapton layer. The heat flux is most sensitive to the temperature measurement, hence the thermocouples were calibrated in a Fluke dry well for the operating conditions they were exposed to with the calibration (R^2 of 0.99995). With the uncertainties in measurement documented in Table 2 the total uncertainty on the heat flux is around 11 %.

Similar to before, the spectrum of the ALTP heat flux and thermocouple are compared from the time signal. The thermocouples show fluctuations at low frequency < 100 Hz, and are similar to the ALTP spectrum as shown in Figure 8. However, due to their slow response, they are unable to capture higher frequency oscillations.

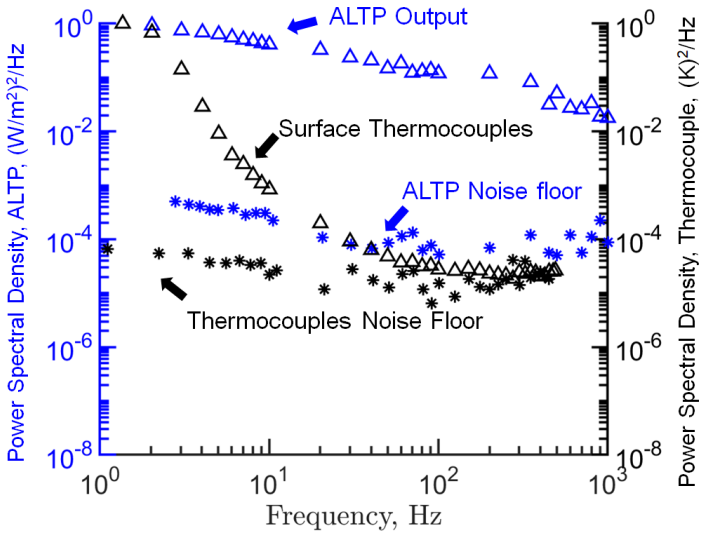

Figure 8: SPECTRAL DENSITY OF THE FLOW EVALUATED FOR THE ALTP AND THE SURFACE THERMOCOUPLE.

4. ASSESSMENT Of CALIBRATION

Results of the radiation-based calibration procedure

Figure 9 shows the calibration curves of the ALTP, HFM-8E and TG-2000 sensors. The calorimeter is not calibrated by laser-radiation because it does not possess a suitable coating with known optical properties. The curves in Figure 9 display the measured sensor voltage output versus the specific radiation intensity. Each point results from three repeated measurements and the deviation is

not shown because it is within the symbol size ($\sigma \pm 1\,\%$). It can be seen that all three sensors have a linear characteristic and the slope of linear regression delivers the sensitivity. All sensitivities measured S_{Exp} in the current setup are shown in Table 3 in comparison with the sensitivities given by the manufacturers S_{Man}. The ALTP has the lowest sensitivity but also a small active film area with $6\,\mathrm{mm}^2$, compared to the HFM-8E and the TG-2000. All sensitivities account for the emissivity of the sensor specific coating (see Instrumentation section). The HFM-8E requires in addition the compensation of the temperature depending sensitivity by means of the measured sensor temperature. The sensitivity is corrected according to the manufacturers manual/calibration.

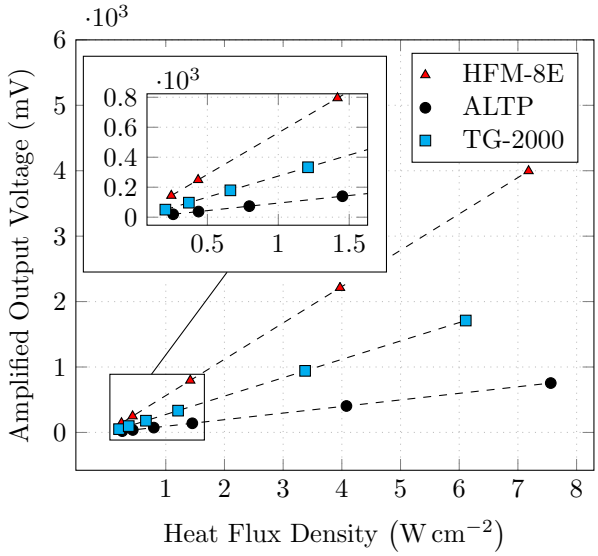

Figure 9: RADIATION-BASED CALIBRATION CURVE FOR TESTED HEAT FLUX SENSORS WITH CONSIDERATION OF THE SPECIFIC EMISSION COEFFICIENT.

The deviation of determined sensitivities and the ones given by the manufacturers is $< 5\,\%$ for all three sensors. The value is much smaller than the overall uncertainty estimation of $\approx 14\,\%$ of the radiation procedure (see section Calibration procedures). Therefore, a good comparability of the sensitivities of radiation-calibrated sensors is given.

Table 3: RESULTS OF THE LASER CALIBRATION PROCESS IN COMPARISON TO THE MANUFACTURERS' CALIBRATION.

Sensor	S_{man}	S_{exp}	Dev.
ALTP	104 $\left(\mu\mathrm{V\,cm^2\,W^{-1}}\right)$	108 $\left(\mu\mathrm{V\,cm^2\,W^{-1}}\right)$	4 %
HFM-8E	576 $\left(\mu\mathrm{V\,cm^2\,W^{-1}}\right)$	562 $\left(\mu\mathrm{V\,cm^2\,W^{-1}}\right)$	3 %
TG-2000	320 $\left(\mu\mathrm{V\,cm^2\,W^{-1}}\right)$	309 $\left(\mu\mathrm{V\,cm^2\,W^{-1}}\right)$	5 %

Figure 10 shows the calibration curve of the coaxial thermocouple as calculated heat flux vs. reference heat flux determined by the power meter. Using the temperature signal of the coaxial thermocouple as input, the Cook-Feldermann (CF) algorithm [5] is applied for heat flux calculation. The calibration curve shows a linear behavior and only slight deviations from the bisectioning line. The results confirm, that the numerical procedure and the thermal parameters are appropriate for his radiation heat load if an appropriate coating with known optical parameters is applied.

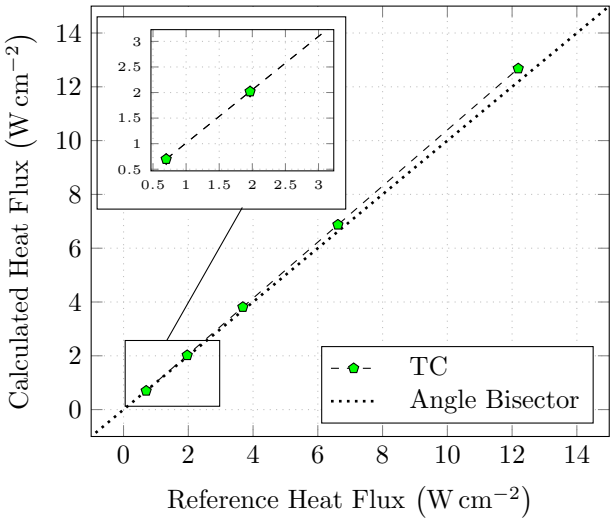

Figure 10: RADIATION-BASED CALIBRATION RESULTS FOR THE COAXIAL THERMOCOUPLE WITH CONSIDERATION OF THE SPECIFIC EMISSION COEFFICIENT IN COMPARISON AGAINST THE REFERENCE LASER SOURCE.

Results of the stagnation point convection-based calibration procedure

The comparison of all sensors (ALTP, HFM-8E, TG-2000, coaxial thermocouple, calorimeter) in the convective environment is made at a fixed point with a constant distance H/D = 5 (corresponding to 240 mm traveling distance of the impinging jet). Figure 11 displays five different time histories which are typical signals during the calibration of the ALTP, HFM-8E, TG-2000, Calorimeter and the coaxial thermocouple, respectively. The Figure 11 (a-c) show the measured output voltage of the heat flux sensors on the right ordinate and the heat flux densities calculated by means of the sensitivity S_{Exp} (see Table 3) obtained from laser calibration on the left ordinate. All signals show the rise of heat flux density after the opening of the shutter (= exposure). The mean value remains approximately constant during the exposure for about 1.5 seconds. The fluctuations during the exposure result from the turbulence of the free jet which are resolved differently due to the specific time constants of the heat flux sensors

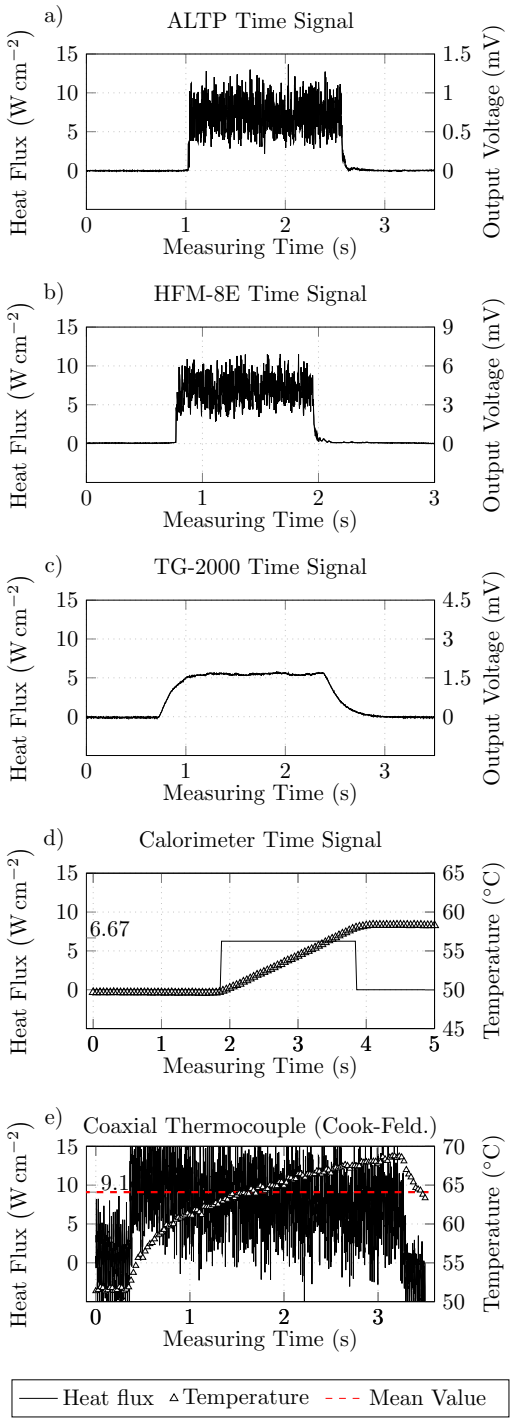

Figure 11: COMPARISON OF TIME SIGNALS (FILTERED WITH A RUNNING-MEAN FILTER AT 1 kHz) a) ALTP, b) HFM-8E, c) TG-2000, d) COAXIAL THERMOCOUPLE.

(comp. Figure 6). The temporal evolution of the signals will be discussed in detail further below. First, only the mean values will be discussed.

Figure 11 d, e) displays two signals: the temperature signal (right ordinate) of is shown in triangles. The temperature is calculated from measured voltage signals and the standard NIST polynomial approximation, resp. the temperature sensitivity given by the manufacturer. On the one side using a calorimeter and Equation 2 in d) a time averaged heat flux signal can be calculated. Due to the calorimetric principle resulting in a relatively slow response time, turbulence effects can not be observed in the time signal. On the other side using a coaxial thermocouple, the slope of the temperature curve in e) increases rapidly at the beginning, decays afterwards and remains about constant resulting in a linear rise with increasing time. After the end of the exposure the signal declines again. The fluctuations on the signal are mainly originated from the numerical noise produced by the algorithm which can be seen already superimposed on the time signal before exposure (different algorithms and their noise will also be discussed further below). The time progression of the heat flux signal shows a declining trend. This effect might indicate a warming-up of the TC which leads to an increasing invalidity of the semi-infinite wall assumption for longer measurement times which is inherent for the numerical evaluation by the CF technique.

The mean values calculated from 20 repeated measurements and resulting time histories like shown in Figure 11 (a-e) are evaluated. The mean values and its standard deviation σ are shown in Figure 12 for all measurement techniques used. For the ALTP and the HFM-8E sensor, the absolute mean values measured in the stagnation region (st): ALTP: $Q_{\mathrm{st}} = 7.24\,\mathrm{W\,cm^{-2}}$; HFM-8E: $Q_{\mathrm{st}} = 7.11\,\mathrm{W\,cm^{-2}}$ differ only within 2 %. The results are very reproducible with a low deviation of $\sigma = 0.10\,\mathrm{W\,cm^{-2}}$, $0.06\,\mathrm{W\,cm^{-2}}$, respectively. Comparing these results to the calorimeter show a mean value of approximately $Q_{\mathrm{st}} = 6.65\,\mathrm{W\,cm^{-2}}$ which is about $5-7\,\%$ lower with a larger standard deviation of $\sigma = 0.115\,\mathrm{W\,cm^{-2}}$. This can probably be explained by a higher measurement uncertainty of the required time interval Δt measurements for this technique (see Instrumentation section). An additional uncertainty can be the assumption of the lumped capacity model (inhomogeneous temperature distribution is neglected, temporal delay of maximum temperature). Furthermore, higher conductive losses during the heat exposure than theoretically estimated might occur and possible convective losses on the rear side of the calorimeter are also unaccounted for. Considering all the above measurements, the laser calibration seems to be applicable for the convective stagnation point calibration, with an overall uncertainty within the accuracy of the sensor calibration in the radiative facility (comp. Table 1). The comparisons of sensitivities obtained from other manufacturers and calibration facilities suggest good absolute agreement. However, a comparison with e.g. variable-temperature blackbody as a broadband radiant source is not presented in this paper and an offset of the absolute value of the laser calibration cannot be excluded.

The coaxial thermocouple (TC) result can be found in Figure 12. Comparing them against the ALTP and HFM-8E measurements, a mean value of

$Q_{st} = 7.352\,\mathrm{W\,cm^{-2}}$ is measured. The standard deviation of the repeated measurements is $\sigma = 0.142\,\mathrm{W\,cm^{-2}}$. These results fit well into the assumed uncertainty $\pm 10\,\%$ of the laser calibration facility, the manufacturer calibrated thermal product $\pm 2\,\%$ and the repeatability of the convective calibration facility $\pm 1.8\,\%$ and supports the calibration of the ALTP and HFM-8E. However, prior investigations in [46] showed 25% higher heat flux values for the same calibration setup. According to the manufacturer, a possible explanation for these kind of deviations can be long measuring times (the semi-infinite wall assumption is only valid for severals microseconds). The experiments was also repeated for different wall materials (aluminum and stainless steel insert) and initial wall temperatures (20 and 50 °C). For this study a threadable coaxial thermocouple in combination with heat conducting paste in the thread was used to lower thermal contact resistances. This probably reduced the overestimation of the heat flux for this study which leads us to the conclusion that care must be taken when installing a coaxial thermocouple and heat flux sensors in general. This is especially true, if different heat flux sensors are compared and used in different environments with different wall materials.

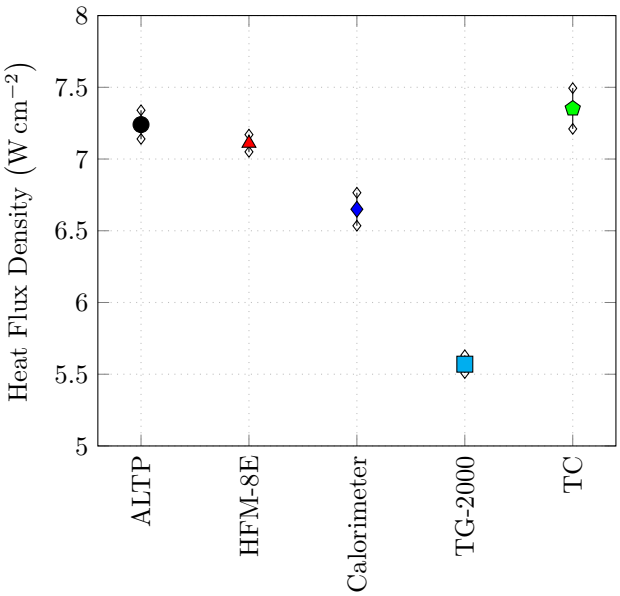

Figure 12: HEAT FLUX DENSITY FOR ALL SENSORS IN THE STAGNATION POINT AT H/D = 5 MEASURED WITH 20 REPETITIONS FOR EACH SENSOR. ERROR INCIDENCES REPRESENTS THE STANDARD DEVIATION.

The results of the circular-foil device in Figure 12 (TG-2000) display lower mean values with an offset of about 20 %. This finding is however consistent with previous studies in a convective environment done by Borell and Diller with 17.7 % deviation [12] and Fu et al. up to 16.9 % [25]. Borell and Diller state that the offset of a circular-foil gage should scale linear with the incident heat

flux, depending on variation of the center-to edge temperature of the sensor. To further investigate this behavior the incident heat flux is varied by shifting the H/D-Distance between 3 and 7.25. To map the exact influence of the varied heat load on the measurement results, the baffle plate is kept at 50 °C. Figure 13 shows the results of the H/D-variation and the decreasing heat flux density in the stagnation point with increasing H/D. The 20 % error-range shows the absolute deviation of the TG-2000 with declining heat flux densities. It indicates that a systematic deviation exists that is direct proportional to the impinging heat flux. This results is in accordance with the measurements of Borell and Diller.

It can be concluded that performing just a radiation calibration without considering the later measurement environment of a heat flux sensors can lead to relatively high systematic errors. Considering this earlier found 20 % offset, the measured heat flux values of the TG-2000 values support the obtained results of the ALTP and HFM-8E.

The H/D-variation is also used in order to study possible non-linearity, temperature/heat flux density dependency effects of the ALTP, the HFM-8E and the TC. Analyzing the ALTP and HFM-8E curves in Figure 13 show that the measured values stay within a 5 % error corridor over the entire H/D-Distance. The TC showed slightly higher deviations for some measurement points but stays well within a 10% interval. It should be noted that only H is varied here for a fixed nozzle diameter D. The HFM-8E has a temperature dependent sensitivity provided by the manufacturer. Within the current heat flux density range, its temperature rise is in the range of 5 to 15 K, the correction effect on the sensitivity ($\Delta S_{\mathrm{man}} = 0.05\,\%\,\mathrm{K}^{-1}$) is very small and hardly noticeable in the calculated heat flux values. These findings indicate that nonlinearity effects are very weak for the present heat loads or are much smaller than the measurement accuracy of the radiation calibration. A major temperature/heat flux dependency of the sensors sensitivity could not be found for all sensors (ALTP, HFM-8E and TC). The findings of Figure 12 and 13 suggest that the sensitivities of the HFM-8E and the ALTP obtained by radiation-based calibration can be directly transfered to a convective environment (for the investigated heat flux range). The TC results support this finding and showed also a good transferability between laser and convection calibration when special attention is given to the installation conditions.

However, it should be noted that sensors with different active sizes are used in the H/D variation in Figure 13. Especially for H/D $>$ 5 the flow uniformity can change and affect the heat flux behavior of techniques with different dimensions. In this study, the core region of the free-jet started to dissolve for H/D $>$ 7.2 that is noticed by a larger disproportionate drop of the TG-2000s heat flux values (sensor with largest active area).

The temporal evolution of the signals (Figure 11) produced by the fluctuations of a free jet and their resulting characteristics are discussed in more detail in the following: The time signals (Figure 11 a, b) of the ALTP and the HFM-8E and the measured fluctuations during exposure seem approximately similar. The rise of the heat flux signal after exposure characterizes only the shutter

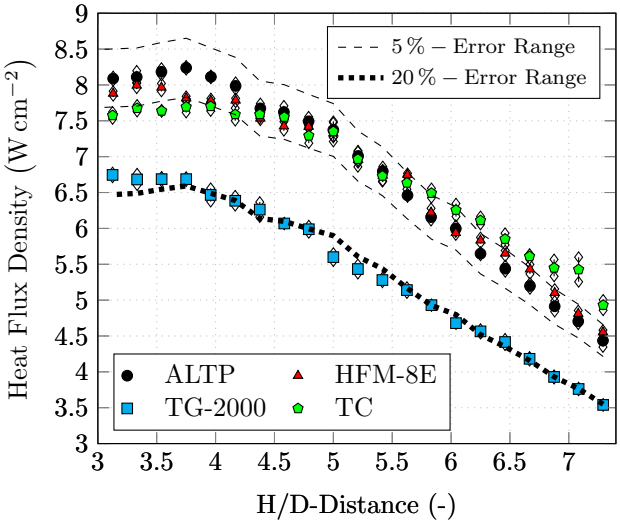

Figure 13: COMPARISON BETWEEN DIFFERENT HEAT MEASURING DEVICES IN THE CONVECTION CALIBRATION FACILITY. ERROR INCIDENCES REPRESENTS THE STANDARD DEVIATION FOR 5 MEASUREMENTS PER DATA POINT.

opening process and does not result from the time constants of the ALTP and HFM-8E. Their time constants are much lower than the opening time of the manual shutter used. The electrical signal noise is very low before the shutter opening, suggesting that the measured fluctuations during the exposure are mainly related to jet flow phenomena of the calibration facility (comp. Figure 6). For signal evaluation, the measured data is numerically filtered with a 1 kHz running-mean filter after recording.

Considering the TG-2000 time history in Figure 11c), the signal characteristic shows significant lower temporal resolution during the exposure and nearly no fluctuations can be resolved. The rise and decay time of this sensor until it reaches 95 % of its maximum or minimum is ≈ 0.2 s, respectively. These times indicate the much lower response time of the sensor which is in accordance to its working principle.

The heat flux signal of the coaxial thermocouple (TC) in Figure 11d) shows significant numerical noise that is produced by the numerical differentiation of the time depending temperature signal. Thus, flow fluctuations can just hardly be distinguished from numerical noise.

Results of the shear flow convection-based calibration procedure.

In the shear flow calibration, the sensors were exposed to a jump in heat flux by passing hot flow over at different flow conditions. Figure 14 shows the change in temperature of the flow and the readings from the instrumentation insert once the valve is opened. The flow is maintained at for 4 minutes to ensure thermal equilibrium. The ALTP response and the heat flux calculated from the

thermocouples are also shown in Figure 14. As stated in the section calibration procedure it should be noted that a different ALTP sensor was used in the LEAF facility due to significant different mounting and operational demands.

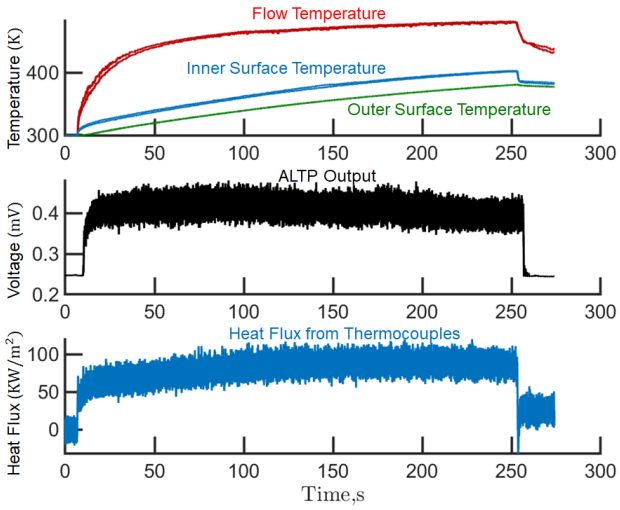

Figure 14: TIME HISTORY OF TEMPERATURE TEMPERATURES FOR A CALIBRATION TEST ALONG WITH ALTP OUTPUT AND HEAT FLUX CALCULATED FROM THERMOCOUPLES.

The facility was characterized for repeatability and stability of conditions. This is highlighted in Figure 15a) which shows the stability of heat flux at three different flow conditions for 20 s of the ALTP compared with the heat flux calculation from the surface thermocouples. Figure 15b) shows the 95 % confidence interval calculated from ten measurement points. The spread is a combination of ALTP measurement fluctuation and fluctuation in the heat flux from the flow.

Comparing the heat flux calculation from the wall temperature and the ALTP output, a linear calibration curve is obtained as shown in Figure 16 a). The calibration line is linear with an R^2 value of 0.9985 and a correlation coefficient of 0.99926 with a sensitivity of 59 µV cm^2 W^{-1}. The relative uncertainty is computed from the methodology presented in [42]. The heat flux density Q is assumed to be with linear behavior of the form of Equation 6.

$$Q = aU + b \tag{6}$$

where a is the slope, U the measured voltage output of the ALTP and b the

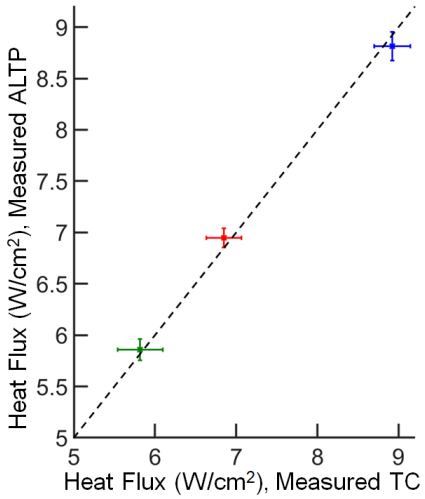

Figure 15: a) STABILITY OF HEAT FLUX b) HOMOGENEITY OF MEASUREMENT SHOWN WITH MEAN OF 10 MEASUREMENTS AND 95 % CONFIDENCE INTERVAL.

intercept of a linear fit. From this linear fit, the slope uncertainty is given by:

$$\Delta a < \frac{t_{\alpha,n-2} s_q \sqrt{1 - r_{qu}^2}}{s_u \sqrt{n-2}} \tag{7}$$

$$\Delta b < \frac{t_{\alpha,n-2} s_q \sqrt{1 - r_{qu}^2} \sqrt{\Sigma_{i=1}^{n} u^2}}{s_u \sqrt{n-2} \sqrt{n}} \tag{8}$$

$$\frac{\Delta Q}{Q} = \sqrt{\left(\frac{Ua}{Q}\right)^2 \left(\left(\frac{\Delta a}{a}\right)^2 + \left(\frac{\Delta U}{U}\right)^2\right) + \left(\frac{b}{Q}\right)^2 \left(\frac{\Delta b}{b}\right)^2} \tag{9}$$

$t_\alpha, n-2$ is the student t distribution factor for $(1-\alpha)$ confidence interval and n number of samples. s_q and s_u are the sample average square of deviations of heat flux density Q and voltage U.

The slope and offset uncertainty are estimated based on the work of Bornstein and Smendjajew [47], shown in Equation 7 and 8. Combining based on Moffat [45], the relative uncertainty of the heat flux is defined as Equation 9. The relative heat flux uncertainty is the uncertainty of the heat flux in percentage of the given heat flux value and is plotted in Figure 16 b). Relative uncertainty is higher for low values of heat flux, approximately 25 % for $1\,\mathrm{W\,cm^{-2}}$ but drops to 8 % at $4\,\mathrm{W\,cm^{-2}}$.

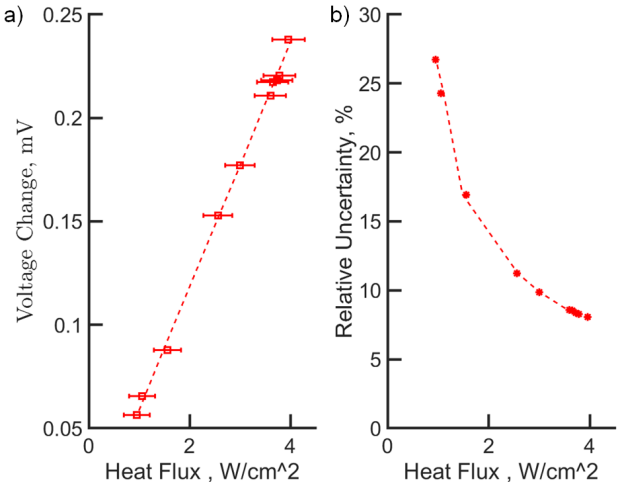

Figure 16: A) ALTP CALIBRATION CURVE WITH UNCERTAINTY BAND, B) RELATIVE UNCERTAINTY OF CALIBRATION POINT [42].

5. APPLICATION OF ALTP SHOCK BOUNDARY LAYER INTERACTION

The linear behaviour and high frequency response makes the ALTP an ideal sensor to measure heat flux in highly unsteady flows. The selected test case is a supersonic nozzle with surface features conducive to complex shock-boundary layer interaction patterns. Details about the geometry and flow field are given by Braun et al. [48]. Tests were performed in the LEAF test section at Purdue University's PETAL lab. Fig 17a) shows the installed test section in the LEAF wind tunnel and Fig 17b) shows the mach contour inside the test section and the position of the ALTP.

The ALTP is mounted at the top wall at the end of the nozzle exposed to flow at Mach 2. The objective for the ALTP was to characterize the initial shock wave that passes during the starting of the nozzle and measure the temporal behaviour of the downstream shock-boundary layer interaction (SBLI). Multiple runs were carried out and to reduce the upstream pressure requirement, testing was done at sub-ambient pressure conditions. The frequency response is used to assess the frequency of the SBLI. Figure 17c) shows the pre-multiplied spectrum with the frequency and the Strouhal number in terms of the first separation shock length. The first two peaks at 232 Hz(St 0.017) and 292 Hz(St 0.021) are attributed to the interaction of the first and second SBLI. These dominant low and mid frequency components are identified due to shock oscillations and separation bubble breathing.

The shock oscillation frequencies are well correlated with the breathing motion of the separation bubble as identified by Deshpande and Poggie [50] who also demonstrated the mechanism of the same. Fisher et al. [49] demonstrated the presence of these oscillations experimentally for the same test article.

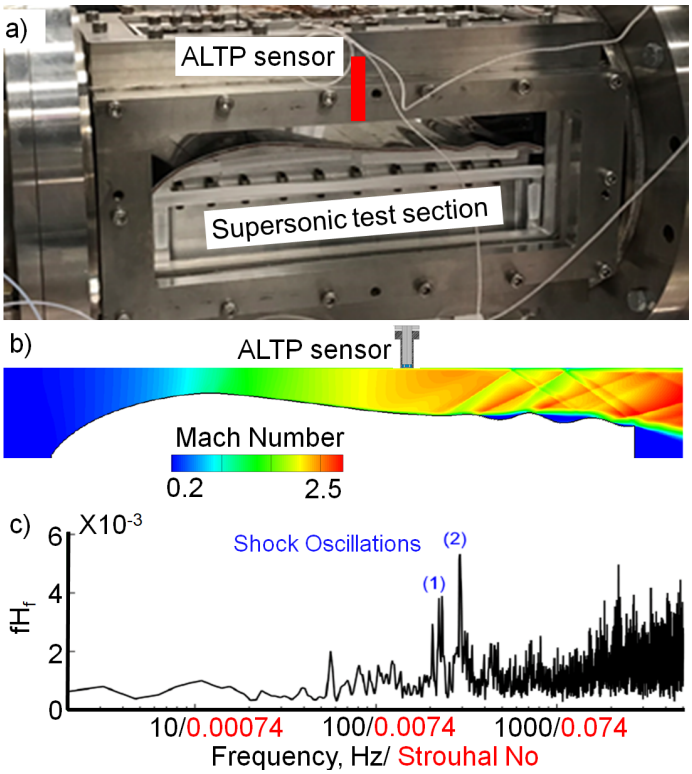

Figure 17: A) TEST ARTICLE MOUNTED IN THE LEAF FACILITY SHOWING THE POSITION OF THE ALTP, B) MACH CONTOUR INSIDE THE TEST ARTICLE RECONSTRUCTED FROM CFD DATA PROVIDED BY FISHER ET AL. [49].

The mean signal was used to assess the heat flux at the starting of the nozzle and at test condition. Figure 18a) shows the evolution of the temperature signal once the flow is started. Figure 18b) and c) show the ALTP response and the heat flux from the thermocouple, respectively. It can be seen that the thermocouples miss the initial jump in heat flux due to the starting shock, as shown, but also are unable to stabilize in the short duration of the test. The averaging window marked in Figure 18b) and c) after the shock has passed at approx. 0.415 s is used to compare the mean heat fluxes. Here, we see a difference of $1\,\mathrm{W\,cm^{-2}}$ in the mean heat flux level for the shown window. The jump in heat flux due to initial shock is compared with URANS simulation performed by Braun et al. [48]. The experimentally measured flow conditions are used as boundary conditions and the spike in heat flux due to the crossing in the supersonic regime is predicted and matches with the data from the ALTP, as shown in Figure 18d). This is not seen in the heat flux from the surface thermocouples.

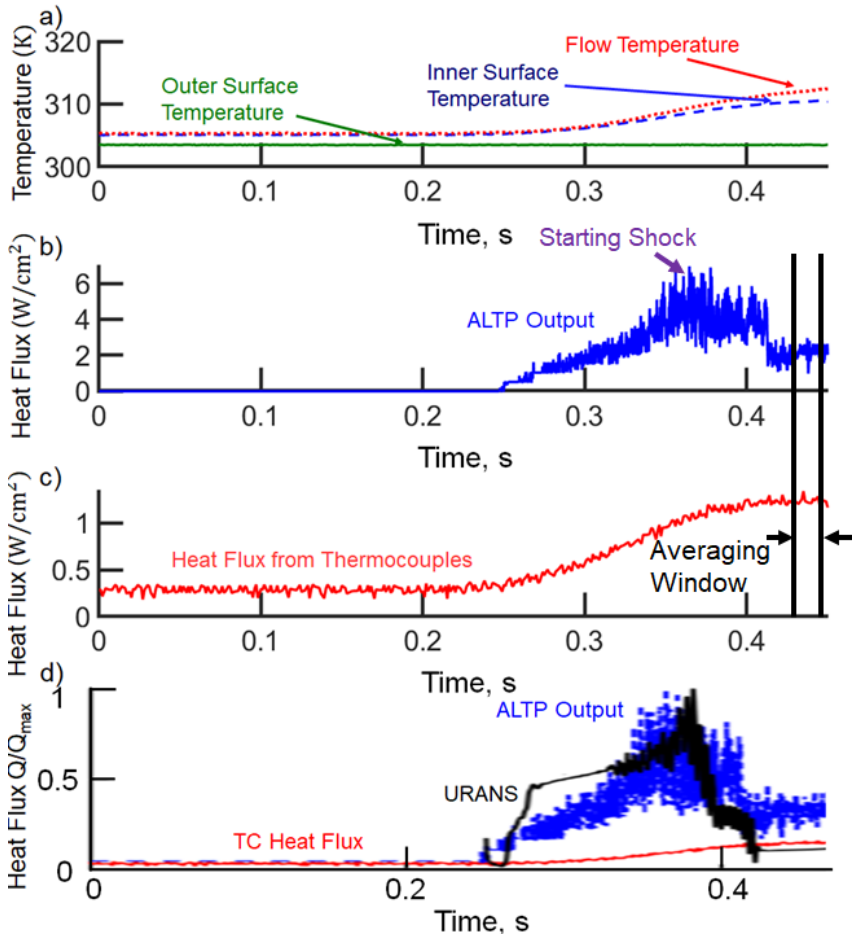

Figure 18: A) TEMPERATURE DATA FROM THERMOCOUPLES, B) HEAT FLUX MONITORED BY ALTP, C) HEAT FLUX MEASURED BY THE THERMOCOUPLES, D) HEAT FLUX FROM ALTP, THERMOCOUPLES, URANS [48].

6. CONCLUSION

The static calibration of different heat flux sensors in a radiation- and convection-based procedure shows measurement principle depending significant, systematic deviations. Thus, a sensitivity transfer between a radiation-calibrated sensor for measurements in convective environments seems not possible for all studied heat flux sensors in a range up to approximately $8\,\mathrm{W\,cm^{-2}}$. In a first step, all radiation-calibrated sensors (Transverse-Seebeck-effect based ALTP, differential layer device HFM-8E, circular-foil gage TG-2000) are calibrated in the same laser-radiation based facility. The determined absolute sensitivities show only $< 5\%$ deviation from the static sensitivities provided by the different manufacturers. The accuracy of the radiation-calibration process is estimated

at about 14 %.

Afterwards, the sensors are compared in a convection-dominated facility that uses stagnation-point measurements of an impinging hot air jet. The homogeneity and repeatability of the procedure is experimentally determined with about 2 % of the mean heat flux density, which makes the facility good for comparative substitution calibration.

The mean values measured by the ALTP and HFM-8E show only a deviation of 5% over the entire heat flux range and no temperature or heat flux density dependent sensitivity changes could be detected. Taking these mean values as reference, the calorimeter delivers an about 5 % lower mean value for a fixed distance (H/D = 5). The TG-2000 indicates a mean value that is about 20 % lower. This is in accordance with results of previous studies for circular-foil gages. A coaxial thermocouple displays a ≈ 5 % higher value than the ALTP/HFM-8E for the same fixed distance. Great care has to be taken when it comes to mounting coaxial thermocouples. It is highly recommended to minimize heat conducting problems in the radial direction, otherwise significantly higher or lower heat flux readings are obtained within the same calibration conditions [46]. These findings show that a comparison of sensitivities in a convective environment is of great importance for the application of heat flux sensors.

The time histories resulting from the exposure to the free hot air jet show the different temporal resolutions of the heat flux sensors. The signal characteristics confirm the benefits of direct heat flux measuring techniques. Temperature-based methods suffer from the numerical noise produced by heat flux calculating algorithms, even if noise reducing procedures are implemented. This is also seen in the shear flow calibration technique where the sensor was calibrated against heat flux extracted from surface thermocouple readings. The heat flux calculation is highly sensitive to the temperature measurement. In practice it is shown the ALTP time response helps it to obtain closer absolute heat flux reading to the true value for short duration and high speed flows. This allows for capturing unsteady phenomenon that will be missed by using temperature-based methods.

Acknowledgement

This research is supported by the German Federal Ministry of Economical Affairs and Energy within the project ZIM ZF4515201 PO7. The authors greatly appreciate the cooperation with Dr. J. Betz (FORTECH HTS) for the development of specific ALTP prototypes. The authors also thank the US Department of Energy for the appointment of Prof. Paniagua to the Faculty Research Participation Program at the NETL.

References

[1] S. P. Schneider, R. Bowersox, Hypersonic Transition and Turbulence, Encyclopedia of Aerospace Engineering, John Wiley & Sons, Ltd, 2010.

[2] D. Lejsek, A. Kulzer, Investigations on the transient wall heat transfer at start-up for si engines with gasoline direct injection, SAE International Journal of Engines 2 (1) (2009) 381–397.

[3] L. Weiss, M. Wensing, N. Engel, H. W. Höppel, F. Siegel, R. Meske, M. Tilinski, D. Zülow, L. Passily, Local heat transfer and interdependency of piston material, spray and combustion in high power diesel engines, in: Leipertz A., Fröba A. P. (Eds.), Engine Combustion Processes and Alternative Concepts, Vol. 19.1, 2019.

[4] S. C. Jenkins, J. von Wolfersdorf, B. Weigand, T. Roediger, H. Knauss, E. Kraemer, Time-resolved heat transfer measurements on the tip wall of a ribbed channel using a novel heat flux sensor—part II: Heat transfer results, Journal of Turbomachinery 130 (1) (2010) 9.

[5] W. J. Cook, Felderman E. J., Reduction of data from thin-film heat-transfer gages - a concise numerical technique, AIAA Journal 4 (3) (1966) 561–562.

[6] D. N. Kendall, P. W. Dixon, Heat transfer measurements in a hot shot wind tunnel, IEEE Trans. Aerosp. Electron. Syst. (1966) 596–603.

[7] T. E. Diller, Methods of determining heat flux from temperature measurements, in: Proceedings of the 42nd International Instrumentation Symposium, Aerospace Industries Division and Test Measurement Division of ISA, 1996.

[8] T. Roediger, H. Knauss, J. Srulijes, F. Seiler, E. Kraemer, A novel fast-response heat-flux sensor for measuring transition to turbulence in the boundary layer behind a moving shock wave, in: Shock Waves, Vol. 27, Springer Berlin Heidelberg, 2009, pp. 415–420.

[9] T. Rödiger, H. Knauss, B. V. Smorodsky, M. Estorf, S. P. Schneider, Hypersonic instability waves measured using fast-response heat-flux gauges, AIAA: Journal of Spacecraft and Rockets 46 (2) (2009) 266–273.

[10] M. A. Kegerise, S. J. Rufer, Unsteady heat-flux measurements of second-mode instability waves in a hypersonic boundary layer, in: 54th AIAA Aerospace Sciences Meeting 2016, Curran Associates Inc, Red Hook, NY, 2016, p. 266.

[11] Vatell Corporation, HFM-6, HFM-7, & HFM-8 operator's manual: , webpage accesed 12/01/2019 (2015).

[12] G. J. Borell, T. E. Diller, A convection calibration method for local heat flux gages, Journal of Heat Transfer 109 (1) (1987) 83.

[13] R. J. Moffat, C. Danek, Final report: The NIST/NSF workshop on heat flux transducer calibration., at NIST in Gaithersburg, MD 1995.

[14] B. K. Tsai, C. E. Gibson, A. V. Murthy, E. A. Early, D. P. Dewitt, R. D. Saunders, NIST measurement service: Heat-flux sensor calibration (2004).

[15] A. V. Murthy, B. K. Tsai, C. E. Gibson, Calibration of high heat flux sensors at NIST, Journal of research of the National Institute of Standards and Technology 102 (4) (1997) 479–488.

[16] A. V. Murthy, B. K. Tsai, R. D. Saunders, High-heat-flux sensor calibration using black-body radiation, Review of Scientific Instruments 35 (4) (1998) 501–504.

[17] T. Roediger, The atomic layer thermopile: A new heat transfer measurement technique in fluid mechanics and thermodynamics: doctoral thesis, Univ. Stuttgart, 2010.

[18] L. Bhatnagar, G. Paniagua, Development of high speed and high temperature atomic layer thermopiles, in: Proceedings of the ASME Turbo Expo, The American Society of Mechanical Engineers, New York, N.Y., 2019.

[19] D. G. Holmberg, T. E. Diller, High-frequency heat flux sensor calibration and modeling, Journal of Fluids Engineering 117 (4) (1995) 659–664.

[20] J. M. Hager, S. Simmons, D. Smith, S. Onishi, L. W. Langley, T. E. Diller, Experimental performance of a heat flux microsensor, Journal of Engineering for Gas Turbines and Power 113 (2) (1991) 246–250.

[21] J. M. Hager, S. Onishi, L. W. Langley, T. E. Diller, Heat flux microsensors, Heat transfer measurements, analysis and flow visualization (1989).

[22] A. Wagner, E. Schülein, R. Petervari, K. Hannemann, S. R. C. Ali, A. Cerminara, N. D. Sandham, Combined free-stream disturbance measurements and receptivity studies in hypersonic wind tunnels by means of a slender wedge probe and direct numerical simulation, Journal of Fluid Mechanics 842 (2018) 495–531.

[23] A. V. Murthy, B. K. Tsai, R. D. Saunders, Radiative calibration of heat-flux sensors at nist: Facilities and techniques, Journal of research of the National Institute of Standards and Technology 105 (2) (2000) 293–305.

[24] A. V. Murthy, G. T. Fraser, D. P. DeWitt, A summary of heat-flux sensor calibration data, Journal of research of the National Institute of Standards and Technology 110 (2) (2005) 97–100.

[25] T. Fu, A. Zong, Y. Zhang, H. S. Wang, A method to measure heat flux in convection using gardon gauge, Applied Thermal Engineering 108 (2016) 1357–1361.

[26] J. C. Yang, Transient analysis of a circular foil gage in a convective and radiative environment, International journal of thermal sciences 130 (2018).

[27] D. E. Smith, J. V. Bubb, O. Popp, T. E. Diller, S. J. Hevey, A comparison of radiation versus convection calibration of thin-film heat flux gauges., HTD-Proceedings of the ASME Heat Transfer Division 1999 (364-4) 79–84.

[28] T. Roediger, H. Knauss, S. Wagner, E. Krämer, The atomic layer thermopile - a fast heat flux sensor for measuring high heat loads in short duration hypersonic ground testing facilities, Proc. ICMAR (1) (2007) 154–166.

[29] Mueller Instruments GmbH & Co.KG, Brochure heat flux thermocouple MCT (2019).

[30] K. F. Renk, J. Betz, S. Zeuner, H. Lengfellner, W. Prettl, Thermopile effect due to laser radiation heating in thin films of high-Tc materials, Physica C: Superconductivity 235-240 (1994) 37–40.

[31] H. Knauss, T. Roediger, U. Gaisbauer, E. Kraemer, D. Bountin, B. Smorodsky, A. Maslov, J. Srulijes, F. Seiler, A novel sensor for fast heat flux measurements, in: 25th AIAA Aerodynamic Measurement Technology and Ground Testing Conference, American Institute of Aeronautics and Astronautics, Reston, Virigina, 2006, p. 102.

[32] ForTech HTS GmbH, Users manual, ultrafast heat transfer sensor: ALTP (2019).

[33] X. Song, K. Huan, W. Dong, J. Wang, Y. Zang, X. Shi, Research on infrared radiation characteristics of Pyromark1200 high-temperature coating, in: M. Guina, H. Gong, Z. Niu, J. Lu (Eds.), International Symposium on Optoelectronic Technology and Application 2014: Infrared Technology and Applications, SPIE Proceedings, SPIE, 2014, p. 93001S.

[34] J. Song, X. P. Hao, Z. D. Yuan, Z. L. Liu, L. Ding, Research of ultrablack coating emissivity based on a controlling the surrounding radiation method, International Journal of Thermophysics 39 (7) (2018) 7.

[35] R. Gardon, An instrument for the direct measurement of intense thermal radiation, Review of Scientific Instruments 24 (5) (1953) 366–370.

[36] T. Fu, A. Zong, J. Tian, C. Xin, Gardon gauge measurements of fast heat flux transients, Applied Thermal Engineering 100 (2016) 501–507.

[37] Vatell Corporation, TG-2000 operator's manual: , webpage accesed 12/01/2019 (2019).

[38] H. Olivier, Thin Film Gauges and Coaxial Thermocouples for Measuring Transient Temperatures, Shock Wave Laboratory: Aachen, 2003.

[39] J. Saavedra, G. Paniagua, B. H. Saracoglu, Experimental Characterization of the Vane Heat Flux Under Pulsating Trailing-Edge Blowing, Journal of Turbomachinery 139 (6) (2017) 061004.

[40] V. Pinilla, J. P. Solano, G. Paniagua, R. J. Anthony, Adiabatic Wall Temperature Evaluation in a High Speed Turbine, Journal of Heat Transfer 134 (9) (2012).

[41] G. Paniagua, D. Cuadrado, J. Saavedra, V. Andreoli, T. Meyer, J. P. Solano, R. Herrero, S. Meyer, D. Lawrence, Design of the Purdue Experimental Turbine Aerothermal Laboratory for Optical and Surface Aerothermal Measurements, Journal of Engineering for Gas Turbines and Power 141 (1) (2019) 012601.

[42] L. Bhatnagar, G. Paniagua, Development of High Speed and High Temperature Atomic Layer Thermopiles, in: Volume 6: Ceramics; Controls, Diagnostics, and Instrumentation; Education; Manufacturing Materials and Metallurgy, American Society of Mechanical Engineers, Phoenix, Arizona, USA, 2019, p. V006T05A014.

[43] L. Bhatnagar, G. Paniagua, D. G. Cuadrado, P. A. N. Aye-Addo, A. Castillo Sauca, F. Lozano, M. Bloxham, Uncertainty in High-Pressure Stator Performance Measurement in an Annular Cascade at Engine-Representative Reynolds and Mach, Journal of Engineering for Gas Turbines and Power 144 (2) (2022) 021001.

[44] H. Schlichting, Boundary-Layer Theory, 7th Edition, McGraw Hill, New York, U.S.A., 1979.

[45] R. J. Moffat, Describing the uncertainties in experimental results, Experimental Thermal and Fluid Science 1 (1) (1988) 3–17.

[46] K. Huber, T. Rödiger, Comparison of radiation and convection-based calibration of fast-response heat flux sensors, in: Proceedings of the ASME Turbo-Expo 2020, ASME, 2021.

[47] I. Bornstein, Semendjajew, K., Tuschenbuch der Marhemafik, Harry Deutsch. Thun, 1980.

[48] J. Braun, G. Paniagua, F. Falempin, Aerothermal Optimization of Bladeless Turbines, Journal of Engineering for Gas Turbines and Power 143 (3) (2021) 031023.

[49] J. M. Fisher, J. Braun, T. R. Meyer, G. Paniagua, Application of femtosecond laser electronic excitation tagging (FLEET) velocimetry in a bladeless turbine, Measurement Science and Technology 31 (6) (2020) 064005.

[50] A. S. Deshpande, J. Poggie, Large-scale unsteadiness in a compression ramp flow confined by sidewalls, Physical Review Fluids 6 (2) (2021) 024610.